

# **Metasurface-based Terahertz Three-dimensional Holography Enabled by Physics-Informed Neural Network**

*Jingzhu Shao, Ping Tang, Borui Xu, Xiangyu Zhao, Yudong Tian, Yuqing Liu, and Chongzhao Wu\**

Center for Biophotonics, Institute of Medical Robotics, School of Biomedical Engineering, Shanghai Jiao Tong University, Shanghai 200240, China

## **KEYWORDS**

metasurface, three-dimensional holography, terahertz, inverse design, deep neural network

## **ABSTRACT**

Artificial intelligence, an emerging, powerful and efficient computational tool, has played a crucial role in the design of optical devices. For the design of holographic metasurfaces, traditional algorithms require multiple iterations between the metasurface and target planes, resulting in excessive computation time. Here, a physics-informed neural network (PINN) is proposed for the fast design of terahertz three-dimensional (3D) holographic metasurfaces. Trained in a self-supervised manner, the PINN eliminates the need for paired input-label datasets. After training, the PINN enables end-to-end mapping between the target holographic patterns and metasurface structures. Both simulation and experimental results of single-plane and 3D multi-plane holography demonstrate that metasurfaces designed by PINN offer higher imaging quality than traditional iterative algorithms. Moreover, the PINN can find approximate solutions of metasurface structures even in physically counterintuitive scenarios, where the holographic patterns of two parallel imaging planes are completely distinct. Furthermore, the inference process of PINN typically takes less than 1 second, much faster than the traditional algorithms requiring iterative computation. Notably, the PINN simultaneously accounts for both phase and amplitude modulation, thereby outperforming traditional phase-only modulation algorithms in handling complex physical scenarios and offering superior imaging quality. This end-to-end design approach has the potential to pave the way for the realization of high-quality, real-time, and large-scale terahertz 3D holographic display technology.

## 1. INTRODUCTION

Computer-generated holography (CGH) enables the recording and reconstruction of light fields by numerically calculating holographic interference patterns (phase information) and encoding them into surface structures or spatial light modulators (SLMs).<sup>1,2</sup> Compared to conventional optical holography, CGH eliminates the reliance on physical interference systems and real objects, enabling a broader application. Currently, CGH has been playing a key role in various fields such as augmented reality (AR), virtual reality (VR), 3D display, and data storage.<sup>3-6</sup> In the terahertz (THz) wave band, although SLMs have been used to generate THz holograms,<sup>7,8</sup> current THz spatial modulation technology is still limited by the weak interaction between traditional optical materials and THz waves.<sup>9</sup> Commercially available products have not been widely adopted yet, which restricts the practical applications of THz SLM.<sup>10</sup>

Metasurfaces are artificially designed planar optical elements composed of periodic meta-atoms at subwavelength scales.<sup>11</sup> The elaborate shapes, materials, and arrangement of these meta-atoms endow them with unique capabilities to manipulate the amplitude, phase, polarization, and other properties of electromagnetic waves, enabling numerous novel functional devices such as multifocal lenses, compact spectrometers, and special beam generators.<sup>12-14</sup> Recently, metasurface-based holography has enabled the generation of diverse holograms ranging from 2D planes to 3D volumes,<sup>15,16</sup> exhibiting broad potential applications in communications, data storage, and display. Meanwhile, holographic metasurfaces operating in the THz band also demonstrate unique value in scenarios including subwavelength-resolution light manipulation, 3D projection, and encrypted display.<sup>9,17-19</sup>

As the functionality of holographic metasurfaces becomes increasingly complex, the difficulty of the design process also rises, especially in the THz band, where the available optical materials and devices remain relatively underdeveloped.<sup>20,21</sup> Conventional numerical calculation methods bear substantial computational burdens while balancing calculation speed and imaging quality. As a representative traditional iterative algorithm, the Gerchberg-Saxton (GS) algorithm converges the phase distribution of the metasurface through multiple round-trip propagations of light fields between the metasurface and the target imaging plane.<sup>22</sup> Though intuitive in concept, it has limitations: computational time surges sharply as the size of the metasurface increases, and it only adapts to phase-only metasurfaces. The neglect of amplitude may lead to compromised imaging quality. Complex amplitude (phase and amplitude) modulation can improve imaging quality and is compatible with sophisticated situations such as 3D and multi-color display, but it exacerbates design complexity.<sup>23</sup> The GS algorithm

requires modification to adapt to this modulation.<sup>24</sup> However, due to unit coupling and errors, as well as crosstalk between amplitude and phase, discrepancies may arise between theoretical calculations and experimental results.<sup>26,27</sup> Therefore, extensive numerical simulations are necessary to screen the structural parameters of meta-atoms and verify the holograms, which further consumes computational resources and increases design difficulty.

With the rapid development of artificial intelligence (AI), deep neural networks (DNNs) have injected new vitality into the design of metasurfaces.<sup>28,29</sup> Leveraging DNNs' data-driven advantages, DNNs can establish an accurate mapping relationship between metasurface geometric structures and electromagnetic response (or target imaging patterns) through massive training data, thereby enabling end-to-end design of holographic metasurface.<sup>26,27</sup> However, such supervised DNNs are essentially regarded as "black-box" models, which lack physical interpretability. It is difficult to clearly link optical principles with the design of metasurface structures in such a framework, which is unfavorable for subsequent optimization and mechanism exploration. Moreover, the performance of DNNs is highly dependent on large-scale paired input-label datasets. The data collection, preprocessing, and model training require significant time investment. Especially in special wavebands such as THz bands, experimental research on related devices is still immature,<sup>30,21</sup> and high-quality experimental data is scarce, which further increases the challenges of such methods. Existing studies have shown that integrating physical models into self-supervised DNNs can not only reduce reliance on paired input-label datasets and improve network training efficiency but also enhance the models' interpretability and design accuracy with the help of prior physical knowledge, opening up a new technical path for the efficient and precise design of holographic metasurfaces.<sup>31-34</sup>

In this work, we propose a physics-informed neural network (PINN) for the rapid inverse design of THz 3D multi-plane holographic metasurfaces. The THz metasurface is composed of silicon pillar meta-atoms with tunable length and width, enabling local complex amplitude modulation of THz waves at the subwavelength level. Three scenarios were designed to verify the feasibility of the PINN, namely single-plane holography, multi-plane holography with identical targets, and dual-plane holography with different targets. The last scenario is particularly challenging, as it contradicts the principle of rectilinear light propagation and defies physical intuition. The GS algorithm was also demonstrated for comparison. The metasurface geometric parameters generated by the PINN algorithm and GS algorithm are used in the Finite-Difference Time-Domain (FDTD) simulation, demonstrating that the PINN algorithm outperforms the GS algorithm in terms of evaluation metrics such as Structural Similarity Index

Measure (SSIM), Normalized Pearson Cross-Correlation (NPCC), and Peak Signal-to-Noise Ratio (PSNR). The metasurface designed by the PINN was fabricated via lithography and dry etching processes, and experimentally verified by the THz quantum cascade laser-based holographic system. The experimental results are consistent with the FDTD simulation results, confirming the feasibility of the PINN. Additionally, the GS algorithm fails in counterintuitive physical scenarios (i.e., dual-plane holography with different targets), while the PINN still finds an approximate solution for the metasurface structural distribution. Furthermore, compared with the GS algorithm, the trained PINN achieves extremely fast metasurface design ( $\sim 1$  second for a  $512 \times 512$  array of metasurface with GPU acceleration). This work will facilitate high-quality, real-time, and large-scale 3D holographic display in the THz band in the future, and provide a valuable reference for the AI-empowered design of THz devices.

## 2. RESULTS AND DISCUSSION

### 2.1. Architecture of the framework

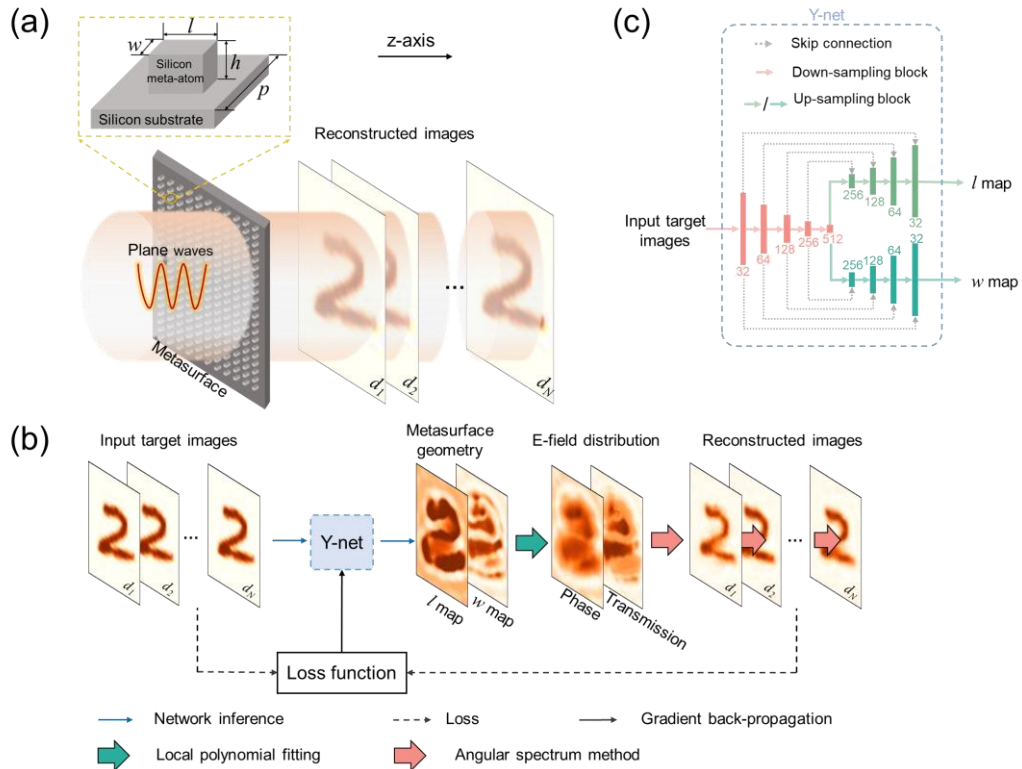


**Figure 1.** The framework for metasurface-based THz 3D holography. (a) Schematic of metasurface-based 3D multi-plane holograms. (b) Self-supervised training pipeline of PINN. (c) Detailed structure of the Y-net.

Figure 1a illustrates the schematic of the all-dielectric metasurface generating 3D multi-plane holograms. A THz plane wave ( $\lambda = 116 \mu\text{m}$ ,  $f = 2.58 \text{ THz}$ ) illuminates the metasurface,

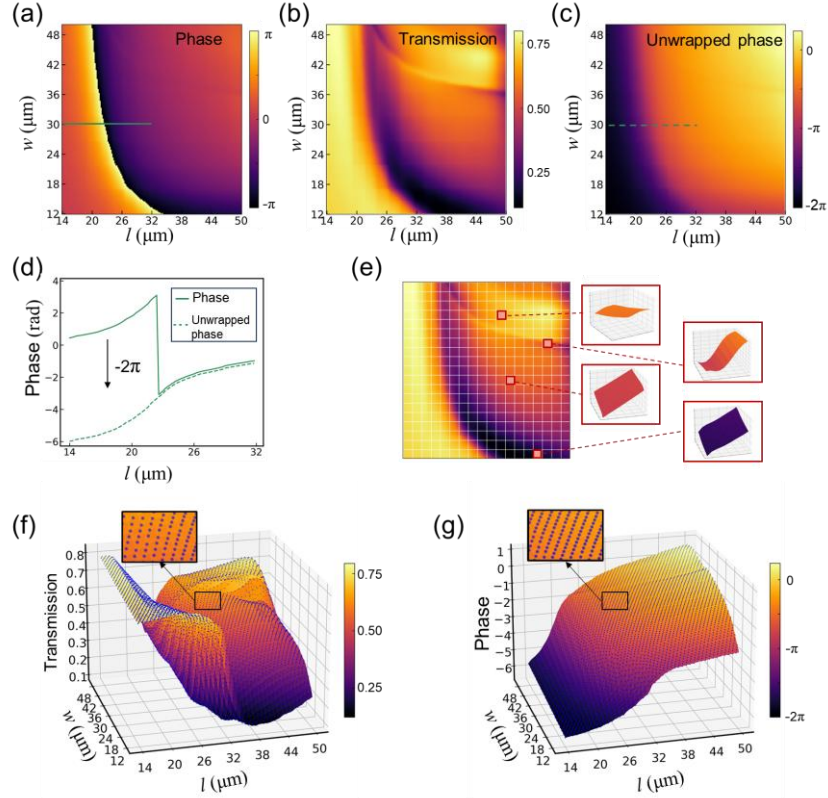
which consists of a  $64 \times 64$  array of silicon pillar meta-atoms on a silicon substrate with a period ( $p$ ) of  $58 \mu\text{m}$ . The meta-atom has a fixed height ( $h$ ) of  $60 \mu\text{m}$ , with the width ( $w$ ) and length ( $l$ ) independently tunable from  $12$  to  $50 \mu\text{m}$  and  $14$  to  $50 \mu\text{m}$ , respectively. This geometric tuning controls the local complex-amplitude response of a single meta-atom. Upon transmitting through the metasurface, the wavefront reconstructs the target images at predefined distances. Symbolic number “2” images at multiple planes along the propagation  $z$ -axis ( $z = d_1, d_2, \dots, d_N$ ), demonstrating the 3D display capability of the designed metasurface.

Figure 1b outlines the self-supervised training pipeline of the proposed PINN. Compared with the supervised training of traditional DNNs, self-supervision can reduce the network’s reliance on paired input-label datasets (i.e., target and geometry datasets). The MINIST datasets serve as input target datasets for the training and testing of PINN (see Methods). The process of self-supervised training begins by feeding the target images at various planes into a Y-shape convolutional neural network termed Y-net, whose detailed encoder-decoder architecture with skip connections is depicted in Figure 1c. The Y-net directly outputs the geometric parameters ( $w$  and  $l$  maps) of the metasurface. A differentiable physical module, which integrates a local polynomial fitting process to map the metasurface geometry to the E-field distribution and the angular spectrum method (ASM) for wave propagation, connects the Y-net’s output to the final reconstructed images. Crucially, the loss function, which quantifies the difference between the input target images and final reconstructed images, is back-propagated to update the Y-net’s weights, enabling an end-to-end, target-to-geometry inference without pre-prepared geometry training data.

### *2.1.1. Local polynomial fitting process*

The local polynomial fitting process (Figure 2) serves as a highly efficient and differentiable surrogate model. It accurately maps the geometry ( $l$  and  $w$ ) of each meta-atom to its complex-amplitude E-field response (phase and transmission) at the near field, effectively replacing computationally intensive full-wave simulations during training. The model is constructed from exhaustive FDTD simulations of a single meta-atom. In the FDTD simulation, a THz plane wave with a wavelength of  $116 \mu\text{m}$  is normally incident on the silicon substrate, passes through the meta-atom, and reaches the detector. Figure 2a and 2b present the phase and transmission response, respectively, obtained by parameter sweeps of the  $w$  ( $12$ - $50 \mu\text{m}$ ) and  $l$  ( $14$ - $50 \mu\text{m}$ ) with a step of  $0.2 \mu\text{m}$ . The phase response in Figure 2a exhibits inherent  $2\pi$  discontinuities that complicate polynomial fitting. To address this, a phase-unwrapping process

was applied, whereby a  $2\pi$  shift was subtracted from data points satisfying the condition of  $w < 36 \mu\text{m}$  and  $\text{phase} > 0$ . This operation converted the discontinuous data (Figure 2a) into a smooth, continuous surface (Figure 2c), which is beneficial for polynomial fitting.



**Figure 2.** Local polynomial fitting. (a-b) FDTD simulation results of phase shift and transmission amplitude of a silicon meta-atom versus its width ( $w$ ) and length ( $l$ ). (c) Unwrapped continuous phase distribution for subsequent local polynomial fitting. (d) Phase unwrapping process to eliminate  $2\pi$  discontinuities. The solid and dashed green lines correspond to the cross-sectional profiles indicated by the green line counterpart in (a) and (c). (e), respectively. Schematic of the local polynomial fitting strategy. (f-g) Results of the local polynomial fitting for transmission and phase, respectively. The discrete blue points represent FDTD data, while the continuous surfaces represent the fitted results.

Instead of global polynomial fitting across the entire parameter space, which would be inaccurate for complicated value distributions, a local polynomial fitting strategy was adopted. As illustrated in Figure 2e, the parameter space is divided into small, localized regions with an array of  $10 \times 10$  pixels. Within each region, a 5th-order polynomial of the form

$$Y = a_0 + a_1 l + a_2 w + a_3 l^2 + a_4 w^2 + a_5 l w + \dots + a_{20} w^5 \quad (1)$$

is then independently fitted to the FDTD data, where  $Y$  represents the transmission or phase distribution within the region, and  $a_0, a_1, a_2, \dots, a_{20}$  are the corresponding local fitting

coefficients. This method transforms the fitting of the complicated global parameter space into a set of simpler, smooth local approximations (Figure 2e), thereby significantly improving fitting accuracy. The results of the local polynomial fitting of the transmission and phase are presented in Figure 2f,g, respectively. The discrete blue dots in the magnified insets represent the FDTD data, while the continuous surfaces show the values predicted by the local polynomial model. The close agreement between the two is quantified by remarkably low Normalized Mean Squared Error (NMSE) of  $2.77 \times 10^{-6}$  for transmission and  $2.17 \times 10^{-6}$  for phase. In contrast, the global fitting approach yields significantly higher errors of  $1.53 \times 10^{-2}$  and  $1.34 \times 10^{-2}$ , respectively. Ultimately, this highly accurate and fully differentiable surrogate model is crucial for the stable and effective training of the PINN.

### 2.1.2. Angular spectrum method

The Angular Spectrum Method (ASM) is employed for its numerical rigor and differentiability, enabling accurate wave propagation modeling. As illustrated in Figure 1c, the ASM calculates the complex-amplitude E-field distribution from the metasurface plane ( $z = 0$ ) to the reconstructed image planes ( $z = d_1, d_2, \dots, d_N$ ). Propagation is implemented sequentially. Starting from  $z = 0$ , the E-field is propagated to the first plane ( $z = d_1$ ). The resulting E-field at  $z = d_1$  then serves as the source for propagation to the next plane ( $z = d_2$ ). This process continues until the E-field at all planes has been computed. The detailed mathematical formulation is described in the Methods section.

### 2.1.3. Loss function

The loss function is designed to quantify the discrepancy between the reconstructed multi-plane images and the input target images, thereby driving the self-supervised learning process. By minimizing this loss through backpropagation, the PINN is iteratively guided to discover the optimal metasurface geometry that generates the desired multi-plane holograms. The total loss  $L_{total}$  is computed as the mean of the individual loss values evaluated at each target plane ( $z = d_1, d_2, \dots, d_N$ ):

$$L_{total} = \frac{1}{N} \sum_{i=1}^N L^{(i)} \quad (2)$$

where  $L^{(i)}$  denotes the composite loss calculated for the  $i$ -th plane. At each plane, a composite loss function  $L^{(i)}$ , is formulated to incorporate constraints on both image shape and optical efficiency, ensuring high-quality holographic imaging while maximizing light utilization (see methods).

## 2.2 Single-plane holography

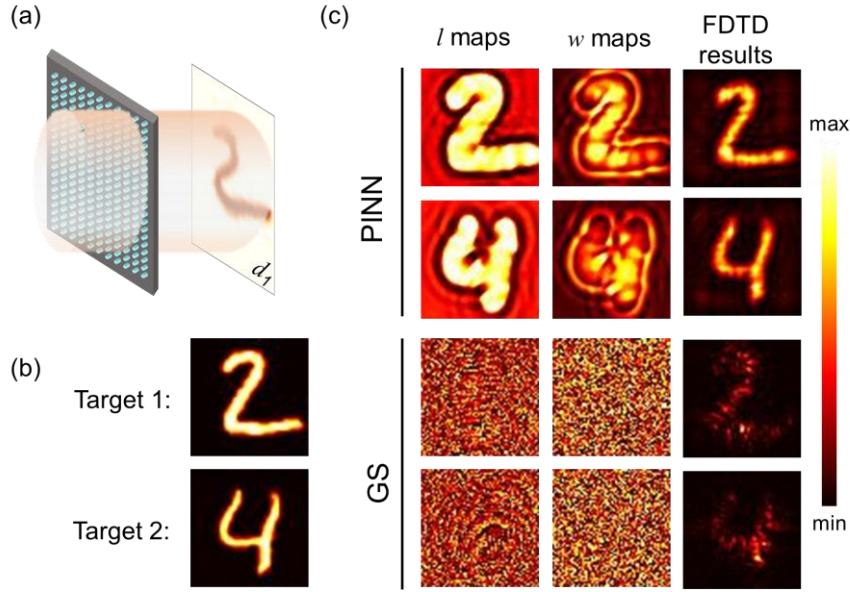


**Figure 3.** Simulation results of single-plane holography. (a) Scenario of metasurface-based single-plane holography. (b) Target images. (c) Length map, width map, and FDTD simulation results of PINN and GS algorithms.

Figure 3 presents the simulation results of single-plane holography (i.e.,  $N = 1$  in the  $d_1, d_2, \dots, d_N$  configuration illustrated in Figure 1). A schematic of the metasurface-based holography for this scenario is depicted in Figure 3a with the imaging plane located at  $d_1 = 3$  mm. The MNIST datasets of handwritten numbers were chosen as the target images for training and testing (see Methods). Two testing targets, the numerals “2” and “4”, are shown in Figure 3b. The targets were input to the trained PINN, which outputs the length ( $l$ ) and width ( $w$ ) maps (Figure 3c). For comparison, the GS algorithm was also employed to design the metasurfaces (3000 iterations). It is worth noting that while the GS algorithm outputs a phase map, which was subsequently converted into  $l$  and  $w$  maps via the mapping relationship, the PINN enables end-to-end metasurface inverse design. The  $l$  and  $w$  maps were utilized in the full-wave FDTD simulation to verify the imaging performance of the metasurface (see Methods). As illustrated in Figure 3c, the images reconstructed by PINN exhibit superior reconstruction quality, showing more uniform intensity distributions inside the target regions. In contrast, the results of the GS algorithm suffer from serious discontinuities and blurred shape boundaries. Quantitative evaluations further confirm the high performance of PINN, using the target images as ground truth to calculate the metrics of PSNR, SSIM, and NPCC (Table 1).

**Table 1.** Quantitative evaluation metrics of PINN and GS algorithms in single-plane holography.

	Algorithms			
	PINN		GS	
	Target 1	Target 2	Target 1	Target 2
NPCC	0.971	0.964	0.778	0.804
SSIM	0.528	0.631	0.281	0.321
PSNR	17.9 dB	19.6 dB	10.8 dB	13.2 dB

The GS algorithm only processes phase information, with the assumption that the amplitude information is fixed. An additional step is required to map the phase information onto the metasurface structure ( $l$  and  $w$  maps). However, this mapping is not reversible, meaning that the metasurface structures designed via the GS algorithm yield non-uniform amplitude distributions. Its neglect of amplitude information directly leads to a degradation in imaging quality. In comparison, the PINN algorithm can directly output the  $l$  and  $w$  maps of the metasurface, enabling direct manipulation of the complex amplitude of light waves. Moreover, due to the random phase initialization strategy, the  $l$  and  $w$  maps derived from the GS algorithm show no direct correlation with the target image (Figure 3c). In contrast, the metasurface structures designed via the PINN algorithm exhibit a certain degree of correlation with the target images (Figure 3c). These reasons explain why the performance of the PINN algorithm is superior to that of the GS algorithm.

Figure 4 presents the experimental setup and results for holographic imaging using metasurfaces designed by PINN. As illustrated in Figure 4a, a collimated beam from a 2.58 THz quantum cascade laser (QCL) illuminates the metasurface, which is mounted on a translation stage. The resulting intensity patterns are then recorded by a THz camera (Swiss Terahertz, Rigi camera). The fabricated metasurface and its scanning electron microscopy (SEM) images are displayed in Figure 4c. The imaging results exhibit a uniform structure and complete contour, accurately reproducing the preset shapes “2” and “4” with high fidelity (Figure 4d). The quantitative analysis for Target 1 and Target 2 is as follows: NPCC of 0.943 and 0.953, SSIM of 0.446 and 0.544, and PSNR of 15.1 dB and 17.8 dB, respectively. The imaging quality of the experimental results of PINN is slightly degraded compared with that of its FDTD simulation results. This phenomenon may be attributed to the relatively high background noise in the experimental results (Figure 4d), which is caused by factors such as experimental thermal noise and optical path errors. Notably, the imaging quality of PINN’s experimental results is

even superior to that of the simulation results of the GS algorithm, which indicates excellent fidelity and a strong correlation between the measured patterns and the intended targets.

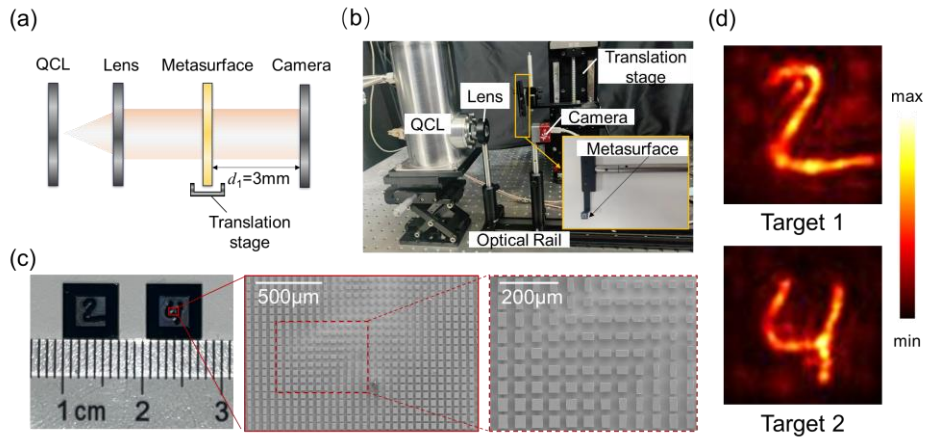


**Figure 4.** Experimental results of single-plane validation. (a) Schematic of the experimental setup. (b) Photograph of the experimental setup. (c) Photograph and SEM images of the fabricated metasurfaces. (d) Measured intensity distributions of the target images.

### 2.3 Multi-plane validation with identical target image

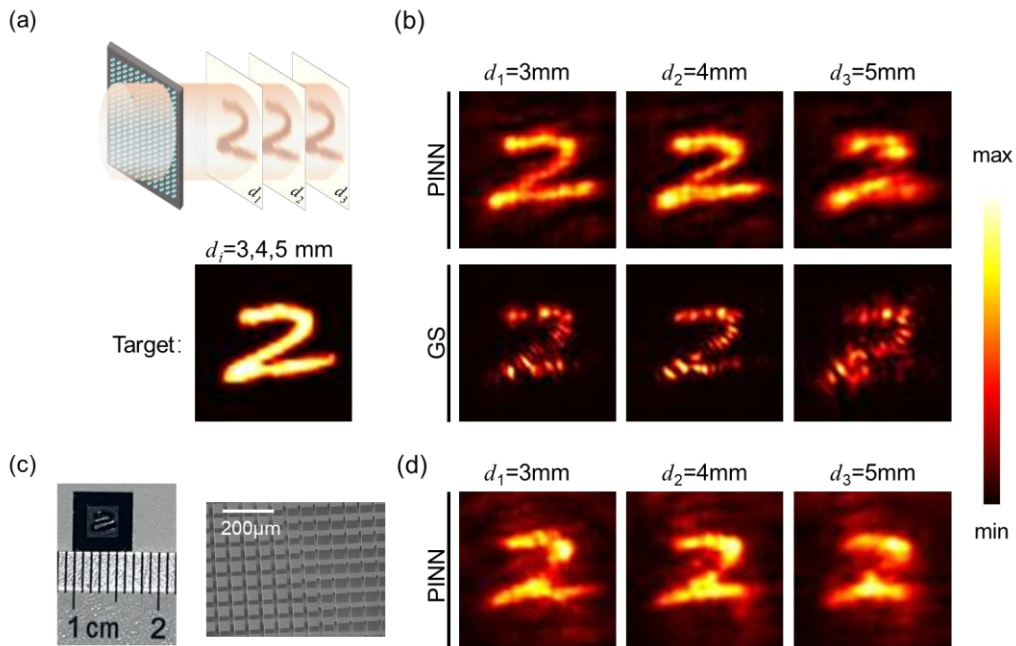


**Figure 5.** Multi-plane 3D validation with an identical target image. (a) Scenario of multi-plane meta-holography and the target image. (b) FDTD simulation results. (c) Photograph and SEM image of the fabricated metasurface. (d) Experimental results.

Figure 5a illustrates the operating scenario of multi-plane metasurface-based holography, where the PINN-designed metasurface is configured to reconstruct identical target images

across planes located at distinct axial distances ( $d_1 = 3$  mm,  $d_2 = 4$  mm,  $d_3 = 5$  mm). It should be noted that the number and spacing of the imaging planes can be flexibly adjusted according to practical scenarios. Figure 5b displays the FDTD simulated results of the PINN algorithm and 3D GS algorithm (3000 iterations) at corresponding axial distances.<sup>19,35</sup> The PINN algorithm clearly reconstructs the outline of the number “2” on each imaging plane, and the light intensity distribution is in high agreement with the target. In contrast, the results of the GS exhibit poor pattern continuity, with the imaging quality deteriorating drastically, especially at  $d_3 = 5$  mm. Quantitatively, the average metrics across the three planes of PINN are: 0.957 (NPCC), 0.601 (SSIM), and 17.6 dB (PSNR). On the other hand, the average metrics of GS decrease to 0.861 (NPCC), 0.402(SSIM), and 12.6 dB (PSNR).

To further validate the practical applicability of the PINN algorithm, the physical experiments were subsequently conducted. The fabricated metasurface designed by PINN is shown in Figure 5c, with a side-view SEM image clearly revealing the meta-atoms arranged on the metasurface. The experimental setup employed herein is consistent with that depicted in Figure 4a,b. Specifically, the metasurface was translated forward and backward along the light propagation direction to acquire the multi-plane imaging data. As shown in Figure 5d, the experimental results exhibit high consistency with the simulated counterparts, thus verifying the feasibility of multi-plane holography using the PINN-designed metasurface. For the experiments, the average metrics across the three planes are summarized as: 0.924 (NPCC), 0.446 (SSIM), and 15.8 dB (PSNR), which are better than the simulation results of the GS algorithm. These results collectively demonstrate that the PINN algorithm can be applied to achieve end-to-end design of high-quality 3D holographic metasurfaces.

#### 2.4. Dual-plane validation with different target images

Figure 6 demonstrates the dual-plane 3D imaging capability of the PINN-designed metasurface with different target images. Figure 6a illustrates the operating scenario: the metasurface is engineered to generate the digit “8” at  $d_1 = 3$  mm and “7” at  $d_2 = 7$  mm. This scenario is physically counterintuitive, as it challenges the principle that light propagates in straight lines in a vacuum environment. A similar physical scenario was demonstrated in Reference 36 using THz metasurfaces. However, in Reference 36, the target patterns on different planes were derived from the same pattern through translation or rotation, thereby achieving a diffraction effect similar to Airy beams. In contrast, the target patterns on the two planes in Figure 6a are only derived from the same MINIST dataset, yet their shapes are entirely

distinct, which renders the realization far more challenging. Figure 6b presents the FDTD simulation results of the PINN algorithm and 3D GS algorithm (3000 iterations). Compared with multi-plane 3D holography with identical patterns, the imaging performance of PINN in this scenario degrades to a certain extent, which is mainly reflected in the increased background noise and reduced uniformity of light intensity in the target pattern regions (Figure 6b). Nevertheless, while the GS algorithm completely fails in this complex scenario, the PINN algorithm can still reconstruct the expected pattern shapes (Figure 6b).

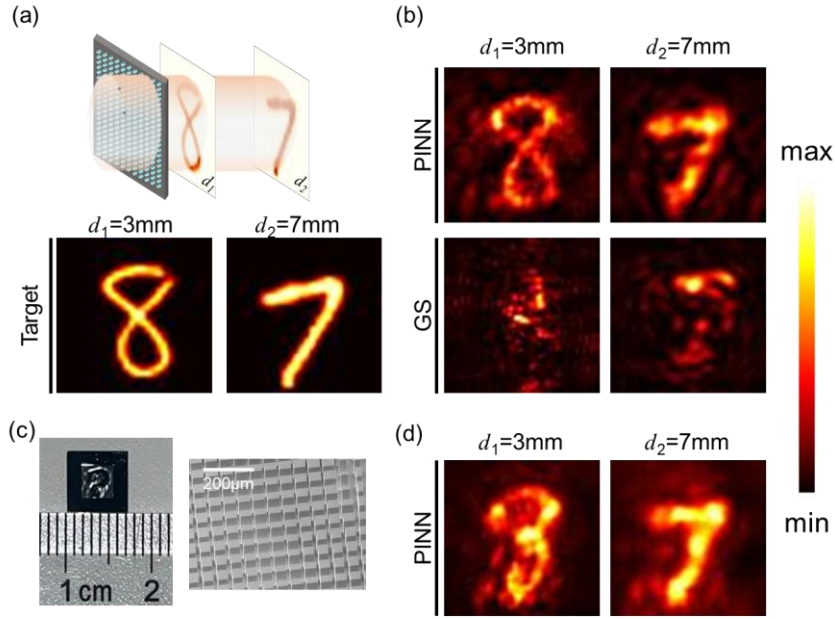


**Figure 6.** Dual-plane validation with different target images. (a) Scenario of dual-plane meta-holography with different target images. (b) FDTD simulation results. (c) Photograph and SEM image of the fabricated metasurface. (d) Experimental results.

The physical experiments were also demonstrated. Figure 6c shows the fabricated metasurface designed by the PINN algorithm. Figure 6d displays the corresponding experimental results, and the target patterns on both planes are successfully reconstructed. Table 2 lists the quantitative evaluation results of the PINN algorithm for both simulation and experiments. Compared with simple physical scenarios (e.g., single-plane holography and multi-plane holography with identical targets), the quantitative evaluation metrics of this scheme exhibit a certain decline, which is inherently determined by the physically unreasonable nature of non-straight light propagation. Nevertheless, some metrics even outperform those of FDTD simulation results of the GS algorithm in simple physical scenarios. This comparison demonstrates the powerful capability of the PINN algorithm in designing metasurfaces for manipulating both simple and sophisticated light fields.

**Table 2.** Quantitative evaluation metrics of PINN in dual-plane holography.

	FDTD simulation		Experiemnt	
	$d_1 = 3$ mm	$d_2 = 7$ mm	$d_1 = 3$ mm	$d_2 = 7$ mm
NPCC	0.903	0.923	0.839	0.908
SSIM	0.460	0.465	0.308	0.343
PSNR	17.5 dB	17.3 dB	15.1 dB	15.4 dB

## 2.5 Computational efficiency

Table 3 presents the computation time of the PINN and GS algorithms across the three aforementioned physical scenarios. It can be observed that the PINN outperforms the GS algorithm in computational efficiency under all scenarios. When only using the CPU (Intel Xeon W-2235), the performance gap between the two algorithms becomes more pronounced in multi-plane holography (2 and 3 planes) and large-area metasurfaces ( $512 \times 512$  meta-atoms). This is because the GS algorithm requires multiple iterations between the metasurface and target planes—multi-plane holography increases the number of target planes, and large-area metasurfaces directly extend the computation time per iteration. In contrast, the PINN only requires inputting the target patterns into the neural networks, and the metasurface structure is obtained in a single inference step. GPU (NVIDIA GeForce RTX 3090) acceleration is beneficial for the design of a large-area metasurface ( $512 \times 512$  meta-atoms). However, the GS algorithm still requires several seconds for iteration. In contrast, the PINN’s computation time can be further compressed to less than 1 second, laying a solid foundation for large-area, real-time 3D displays.

**Table 3.** The computational time of the PINN and GS algorithms.

		Single-plane		Dual-plane (2 planes) with different targets		Multi-plane (3 planes) with identical target	
		PINN	GS	PINN	3D GS	PINNN	3D GS
CPU	$64 \times 64$	0.38s	1.31s	0.38s	2.61s	0.38s	3.99s
	$512 \times 512$	1.12s	14.90s	1.18s	30.02s	1.19s	43.89s
GPU	$64 \times 64$	0.51s	1.04s	0.51s	2.08s	0.52s	3.08s
	$512 \times 512$	0.63s	3.36s	0.60s	6.81s	0.66s	10.33s

## 3. CONCLUSION

In conclusion, we demonstrated the inverse design of a complex-amplitude terahertz metasurface for 3D holography using PINN. The PINN consists of three key components: Y-net, local polynomial fitting, and multi-plane angular spectrum propagation. Taking target images as input, the Y-net can directly output the length ( $l$ ) and width ( $w$ ) maps of the metasurface, enabling fast end-to-end inverse design. The local polynomial fitting process accurately maps the geometric parameters ( $l$  and  $w$ ) of each meta-atom to its complex-amplitude response. As a physical model for light propagation, the angular spectrum method calculates light distribution in a plane-by-plane manner. The PINN allows flexible adjustment of the number and position of holographic planes and the shape of the target patterns as needed. The PINN-based single-plane and multi-plane holography are verified by both FDTD simulations and THz imaging experiments. Compared with the traditional iterative GS algorithm, the PINN achieves faster design speed ( $\sim 1$  second) and generates higher-quality holographic images. This work will benefit the development of high-quality, large-scale 3D holographic display technology in the THz band. Moreover, the proposed method can serve as a universal design framework to obtain the metasurface geometric parameters with various inputs, such as operating wavelength, polarization state, etc. When combined with dynamically metasurfaces, which are tunable by these inputs, it holds great potential for realizing rapid inverse design of photonic devices, thereby achieving real-time 3D holographic display.

## 4. METHODS

### Training Details:

The proposed PINN framework was implemented using Python 3.11.9 and PyTorch 2.1.0. All models were trained on a workstation equipped with an Intel Xeon W-2235 CPU, 64 GB of RAM, and an NVIDIA GeForce RTX 3090 GPU. The training and testing datasets were derived from the MNIST handwritten digit dataset. A total of 10,000 training images and 100 test images were used. All images were resized to  $64 \times 64$  pixels to match the metasurface dimensions, and the pixel values were normalized to a range from 0.01 to 1. For different experimental validations, corresponding datasets were constructed accordingly: (1) For the single-plane validation, both the training and test set were directly randomized to form the images; (2) for the multi-plane validation with identical target image, the same randomized training and test image was assigned to all propagation planes; (3) for the dual-plane validation with distinct target images, the training set was formed by duplicating and randomly shuffling the training images to create unique image pairs for the two planes, with the same procedure

applied to the test dataset. The PINN was trained for 100 epochs using the Adam optimizer with a learning rate of 0.001 and a batch size of 128.

### Loss function:

At each plane, the composite loss function  $L^{(i)}$  is defined by:

$$L^{(i)} = L_{shape}^{(i)} + \alpha L_{light}^{(i)} \quad (3)$$

where  $L_{shape}^{(i)}$  is the shape loss term,  $L_{light}^{(i)}$  is the light efficiency loss term, and  $\alpha$  is a weighting factor that balances the two constraints. The weighting factor  $\alpha$  was set to 0.01. The shape loss term  $L_{shape}^{(i)}$  combines Mean Square Error (MSE) and Normalized Pearson Correlation Coefficient (NPCC) to enforce both pixel-wise accuracy and structural similarity between the reconstructed and target images:

$$L_{shape}^{(i)} = L_{MSE}^{(i)} + L_{NPCC}^{(i)} \quad (4)$$

$$L_{MSE}^{(i)} = \frac{1}{M} \sum \left( I_{tar}^{(i)} - I_{rec}^{(i)} \right)^2 \quad (5)$$

$$L_{NPCC}^{(i)} = 1 - \frac{\sum \left( I_{tar}^{(i)} - \bar{I}_{tar}^{(i)} \right) \cdot \left( I_{rec}^{(i)} - \bar{I}_{rec}^{(i)} \right)}{\sqrt{\sum \left( I_{tar}^{(i)} - \bar{I}_{tar}^{(i)} \right)^2 \cdot \sum \left( I_{rec}^{(i)} - \bar{I}_{rec}^{(i)} \right)^2}} \quad (6)$$

Here,  $I_{tar}^{(i)}$  is the target image intensity,  $I_{rec}^{(i)}$  is the reconstructed image intensity obtained via ASM, and  $M$  is the total number of pixels.  $\bar{I}_{tar}^{(i)}$  and  $\bar{I}_{rec}^{(i)}$  represent the mean intensities of the target and reconstructed images, respectively.

The light efficiency loss  $L_{light}$  is defined as:

$$L_{light}^{(i)} = 1 - \frac{\sum \ln \left( I_{tar}^{(i)} \cdot I_{rec}^{(i)} + 1 \right)}{\sum \ln \left( I_{incident}^{(i)} \right)} \quad (7)$$

where  $I_{incident}^{(i)}$  represents the incident light intensity (assumed to be a plane wave with unit intensity). The logarithmic operation reduces internal contrast variations within the target region, ensuring continuity.

### Angular Spectrum Method (ASM):

Mathematically, the ASM can be formulated as

$$E_{z=d+\Delta d} = \mathcal{F}^{-1} \left[ H \cdot \mathcal{F} \left( E_{z=d} \right) \right] \quad (8)$$

Here,  $E_{z=d}$  and  $E_{z=d+\Delta d}$  represent the scalar components of the E-field at the spatial coordinates  $(x, y, d)$  and  $(x, y, d+\Delta d)$  in 3D space, respectively.  $\mathcal{F}$  signifies the 2D Fourier transformation, which maps the spatial coordinates  $(x, y)$  to the spatial frequency coordinates  $(f_x, f_y)$ . The transfer

function  $H(f_x, f_y)$  that describes the propagation from the plane  $z = d$  to  $z = d + \Delta d$  is calculated as:

$$H(f_x, f_y)|_{\Delta z = \Delta d} = \exp\left(j \frac{2\pi}{\lambda} \Delta d \sqrt{1 - (\lambda f_x)^2 - (\lambda f_y)^2}\right) \quad (9)$$

In this expression,  $\lambda$  denotes the wavelength and  $\Delta d$  denotes the propagation distance between two planes along the optical axis (i.e., z-axis). At each plane, the imaging pattern is the intensity distribution of the E-field:

$$I_z = |E_z|^2 \quad (10)$$

### **Finite-Difference Time Domain (FDTD) Simulation:**

Firstly, the FDTD method (Lumerical FDTD Solutions) was applied to calculate the phase shift and transmission data by sweeping geometric parameters of the meta-atom. In the simulation, a silicon pillar meta-atom was modeled on a silicon substrate. Periodic boundary conditions were applied in the x and y directions, while perfectly matched layers (PMLs) were configured at both the top and bottom boundaries. The height of the silicon pillar was fixed at 60  $\mu\text{m}$ , with the width ( $w$ ) ranging from 12 to 50  $\mu\text{m}$  and the length ( $l$ ) ranging from 14 to 50  $\mu\text{m}$  at a step size of 0.2  $\mu\text{m}$ . A plane wave source ( $\lambda = 116 \mu\text{m}$ ,  $f = 2.58 \text{ THz}$ ) was positioned inside the silicon substrate and beneath the meta-atom, and a frequency-domain field and power monitor was placed above the meta-atom to detect the phase and transmitted power.

Secondly, the FDTD method was applied to calculate the imaging results of the metasurface designed by PINN and GS algorithms. In the simulation, a  $64 \times 64$  array of meta-atoms was arranged on a silicon substrate with a period of 58  $\mu\text{m}$  ( $\lambda/2$ ). The length ( $l$ ) and width ( $w$ ) parameters of each meta-atom were calculated by either the PINN algorithm or the GS algorithm. All boundaries were configured as PMLs. A plane wave source ( $\lambda = 116 \mu\text{m}$ ,  $f = 2.58 \text{ THz}$ ) was placed inside the silicon substrate beneath the metasurface, and a two-dimensional frequency-domain field and power monitor was deployed at the target imaging plane above the metasurface to record the electric field distribution. For 3D holographic imaging simulations, the monitor was placed at each target imaging plane. The obtained electric field data from the monitors were subsequently used to calculate the light intensity distribution generated by the metasurface.

### **Metasurface Fabrication:**

The metasurface was fabricated on a 4-inch high-resistivity silicon wafer (double-side polished, resistance  $> 10000 \Omega$ , thickness = 500  $\mu\text{m}$ ) via a series of microfabrication processes.

Firstly, the silicon wafer is cleaned on a wet cleaning station. Subsequently, pattern transfer is achieved by a contact lithography system with ultraviolet exposure (SUSS-MA8, Germany). Deep silicon etching is then carried out by Deep Reactive Ion Etching (DRIE) technique using SF<sub>6</sub> and C<sub>4</sub>F<sub>8</sub> as process gases, targeting an etch depth of 60 μm (error < 10%). After etching, the photoresist was removed. All metasurface patterns are fabricated uniformly on the silicon wafer. Finally, each metasurface was diced from the silicon wafer by a dicing saw.

### **Experimental Setup:**

The metasurface was characterized using a THz quantum cascade laser (QCL) operating at a wavelength of 116 μm (2.58 THz) with an average output power of ~1.4 mW. The emitted THz wave was collimated into a parallel beam using a TPX lens with a focal length of 25 mm, and was subsequently incident on the metasurface. A THz camera (Swiss Terahertz, Rigi camera) was employed to capture the intensity distribution. The camera features a pixel size of 25 μm and an effective detection area of 3 mm × 4 mm. To fully characterize the multi-plane reconstruction, the camera was sequentially positioned at the respective reconstructed planes ( $z = d_1, d_2, \dots, d_N$ ). Since the incident collimated beam was smaller than the effective modulation area of the metasurface, the sample was mounted on an XYZ-translation stage. By spatially scanning the metasurface relative to the stationary beam, THz signals from different regions were captured and subsequently stitched together to form a complete intensity image at the imaging plane.

## **5. ASSOCIATED CONTENT**

### **Data Availability Statement**

The data and code that support the findings of this study are available from the corresponding author upon reasonable request.

## **6. AUTHOR INFORMATION**

### **Corresponding Author**

Chongzhao Wu – Center for Biophotonics, Institute of Medical Robotics, School of Biomedical Engineering, Shanghai Jiao Tong University, Shanghai 200240, China; orcid.org/0000-0002-5515-3325; Email: czwu@sjtu.edu.cn

## **Authors**

Jingzhu Shao – Center for Biophotonics, Institute of Medical Robotics, School of Biomedical Engineering, Shanghai Jiao Tong University, Shanghai 200240, China; <https://orcid.org/0000-0001-8780-7015>

Ping Tang – Center for Biophotonics, Institute of Medical Robotics, School of Biomedical Engineering, Shanghai Jiao Tong University, Shanghai 200240, China

Borui Xu – Center for Biophotonics, Institute of Medical Robotics, School of Biomedical Engineering, Shanghai Jiao Tong University, Shanghai 200240, China; <https://orcid.org/0000-0003-1212-1646>

Xiangyu zhao – Center for Biophotonics, Institute of Medical Robotics, School of Biomedical Engineering, Shanghai Jiao Tong University, Shanghai 200240, China

Yudong Tian – Center for Biophotonics, Institute of Medical Robotics, School of Biomedical Engineering, Shanghai Jiao Tong University, Shanghai 200240, China

Yuqing Liu– Center for Biophotonics, Institute of Medical Robotics, School of Biomedical Engineering, Shanghai Jiao Tong University, Shanghai 200240, China

## **Author Contributions**

The manuscript was written through contributions of all authors. All authors have given approval to the final version of the manuscript.

## **Funding**

The work is supported by the National Natural Science Foundation of China under Grants 62375170 and 62535019, Shanghai Jiao Tong University under Grant No. YG2024QNA51, the Science and Technology Commission of Shanghai Municipality under Grant No. 20DZ2220400.

## **Notes**

The authors declare no competing financial interest.

## 8. REFERENCES

- (1) Jiang, Q.; Jin, G.; Cao, L. When Metasurface Meets Hologram: Principle and Advances. *Adv. Opt. Photon.* **2019**, *11* (3), 518. <https://doi.org/10.1364/AOP.11.000518>.
- (2) Zang, X.; Yao, B.; Chen, L.; Xie, J.; Guo, X.; Balakin, A. V.; Shkurinov, A. P.; Zhuang, S. Metasurfaces for Manipulating Terahertz Waves. *gxjzz* **2021**, *2* (2), 148–172. <https://doi.org/10.37188/lam.2021.010>.
- (3) Chang, C.; Bang, K.; Wetzstein, G.; Lee, B.; Gao, L. Toward the Next-Generation VR/AR Optics: A Review of Holographic near-Eye Displays from a Human-Centric Perspective. *Optica* **2020**, *7* (11), 1563. <https://doi.org/10.1364/OPTICA.406004>.
- (4) Sahin, E.; Stoykova, E.; Mäkinen, J.; Gotchev, A. Computer-Generated Holograms for 3D Imaging: A Survey. *ACM Comput. Surv.* **2021**, *53* (2), 1–35. <https://doi.org/10.1145/3378444>.
- (5) Blinder, D.; Birnbaum, T.; Ito, T.; Shimobaba, T. The State-of-the-Art in Computer Generated Holography for 3D Display. *gxjzz* **2022**, *3* (3), 572–600. <https://doi.org/10.37188/lam.2022.035>.
- (6) Lin, X.; Liu, J.; Hao, J.; Wang, K.; Zhang, Y.; Li, H.; Horimai, H.; Tan, X. Collinear Holographic Data Storage Technologies. *OEA* **2020**, *3* (3), 190004–190008. <https://doi.org/10.29026/oea.2020.190004>.
- (7) Guo, J.; Wang, T.; Zhao, H.; Wang, X.; Feng, S.; Han, P.; Sun, W.; Ye, J.; Situ, G.; Chen, H.-T.; Zhang, Y. Reconfigurable Terahertz Metasurface Pure Phase Holograms. *Advanced Optical Materials* **2019**, *7* (10), 1801696. <https://doi.org/10.1002/adom.201801696>.
- (8) Xie, Z.; Wang, X.; Ye, J.; Feng, S.; Sun, W.; Akalin, T.; Zhang, Y. Spatial Terahertz Modulator. *Sci Rep* **2013**, *3* (1), 3347. <https://doi.org/10.1038/srep03347>.
- (9) Zhang, Q.; Li, G.; Wu, L.; Yang, F.; Yue, Z.; Zheng, C.; Zhang, Q.; Zhang, C.; Xu, Q.; Tian, Z.; Zhang, Y.; Li, L.; Yao, J. Subwavelength-Resolution Terahertz Hologram with Arbitrary Curved Trajectory and Customized Polarization Structures. *Laser & Photonics Reviews* *n/a* (n/a), e02169. <https://doi.org/10.1002/lpor.202502169>.
- (10) Choporova, Y.; Knyazev, B.; Pavelyev, V. Holography with High-Power CW Coherent Terahertz Source: Optical Components, Imaging, and Applications. *gxjzz* **2022**, *3* (3), 525–541. <https://doi.org/10.37188/lam.2022.031>.
- (11) He, J.; Dong, T.; Chi, B.; Zhang, Y. Metasurfaces for Terahertz Wavefront Modulation: A Review. *J Infrared Milli Terahz Waves* **2020**, *41* (6), 607–631. <https://doi.org/10.1007/s10762-020-00677-3>.
- (12) Xu, B.; Wei, W.; Tang, P.; Shao, J.; Zhao, X.; Chen, B.; Dong, S.; Wu, C. A Multi-Foci Sparse-Aperture Metalens. *Advanced Science* **2024**, *11* (19), 2309648. <https://doi.org/10.1002/advs.202309648>.
- (13) Tang, F.; Wu, J.; Albrow-Owen, T.; Cui, H.; Chen, F.; Shi, Y.; Zou, L.; Chen, J.; Guo, X.; Sun, Y.; Luo, J.; Ju, B.; Huang, J.; Liu, S.; Li, B.; Yang, L.; Munro, E. A.; Zheng, W.; Joyce, H. J.; Chen, H.; Che, L.; Dong, S.; Sun, Z.; Hasan, T.; Ye, X.; Yang, Y.; Yang, Z. Metasurface Spectrometers beyond Resolution-Sensitivity Constraints. *Science Advances* **2024**, *10* (49), eadr7155. <https://doi.org/10.1126/sciadv.adr7155>.
- (14) Berini, P. Optical Beam Steering Using Tunable Metasurfaces. *ACS Photonics* **2022**, *9* (7), 2204–2218. <https://doi.org/10.1021/acsp Photonics.2c00439>.
- (15) Zheng, G.; Mühlenernd, H.; Kenney, M.; Li, G.; Zentgraf, T.; Zhang, S. Metasurface Holograms Reaching 80% Efficiency. *Nature Nanotech* **2015**, *10* (4), 308–312. <https://doi.org/10.1038/nnano.2015.2>.
- (16) So, S.; Kim, J.; Badloe, T.; Lee, C.; Yang, Y.; Kang, H.; Rho, J. Multicolor and 3D Holography Generated by Inverse-Designed Single-Cell Metasurfaces. *Advanced Materials* **2023**, *35* (17), 2208520. <https://doi.org/10.1002/adma.202208520>.

- (17) Wang, Q.; Xu, Q.; Zhang, X.; Tian, C.; Xu, Y.; Gu, J.; Tian, Z.; Ouyang, C.; Zhang, X.; Han, J.; Zhang, W. All-Dielectric Meta-Holograms with Holographic Images Transforming Longitudinally. *ACS Photonics* **2018**, *5* (2), 599–606. <https://doi.org/10.1021/acsp Photonics.7b01173>.
- (18) Zhao, H.; Nan, T.; Wang, X.; Liu, S.; Chen, Z.; Sang, Y.; Wang, Y.; Han, C.; Zhang, Y. Decoupling of Phase and Amplitude Channels with a Terahertz Metasurface Toward High-Security Image Hiding. *Laser & Photonics Reviews* **2025**, *19* (1), 2400944. <https://doi.org/10.1002/lpor.202400944>.
- (19) He, J.; Dong, T.; Chi, B.; Wang, S.; Wang, X.; Zhang, Y. Meta-Hologram for Three-Dimensional Display in Terahertz Waveband. *Microelectronic Engineering* **2020**, *220*, 111151. <https://doi.org/10.1016/j.mee.2019.111151>.
- (20) Zhang, H.; Zhang, X.; Xu, Q.; Tian, C.; Wang, Q.; Xu, Y.; Li, Y.; Gu, J.; Tian, Z.; Ouyang, C.; Zhang, X.; Hu, C.; Han, J.; Zhang, W. High-Efficiency Dielectric Metasurfaces for Polarization-Dependent Terahertz Wavefront Manipulation. *Advanced Optical Materials* **2018**, *6* (1), 1700773. <https://doi.org/10.1002/adom.201700773>.
- (21) Ma, Z. T.; Geng, Z. X.; Fan, Z. Y.; Liu, J.; Chen, H. D. Modulators for Terahertz Communication: The Current State of the Art. *Research* **2019**, *2019*. <https://doi.org/10.34133/2019/6482975>.
- (22) Gerchberg, R. A Practical Algorithm for the Determination of Phase from Image and Diffraction Plane Pictures. *Optik* **1972**.
- (23) Zhao, R.; Huang, L.; Wang, Y. Recent Advances in Multi-Dimensional Metasurfaces Holographic Technologies. *Photonix* **2020**, *1* (1), 20. <https://doi.org/10.1186/s43074-020-00020-y>.
- (24) Mu, Y.; Zheng, M.; Qi, J.; Li, H.; Qiu, J. A Large Field-of-View Metasurface for Complex-Amplitude Hologram Breaking Numerical Aperture Limitation. *Nanophotonics* **2020**, *9* (16), 4749–4759. <https://doi.org/10.1515/nanoph-2020-0448>.
- (25) Wang, Q.; Zhang, X.; Xu, Y.; Gu, J.; Li, Y.; Tian, Z.; Singh, R.; Zhang, S.; Han, J.; Zhang, W. Broadband Metasurface Holograms: Toward Complete Phase and Amplitude Engineering. *Sci Rep* **2016**, *6* (1), 32867. <https://doi.org/10.1038/srep32867>.
- (26) Zhu, R.; Wang, J.; Qiu, T.; Yang, D.; Feng, B.; Chu, Z.; Liu, T.; Han, Y.; Chen, H.; Qu, S. Direct Field-to-Pattern Monolithic Design of Holographic Metasurface via Residual Encoder-Decoder Convolutional Neural Network. *OEA* **2023**, *6* (8), 220148–10. <https://doi.org/10.29026/oea.2023.220148>.
- (27) Zhu, R.; Wang, J.; Fu, X.; Liu, X.; Liu, T.; Chu, Z.; Han, Y.; Qiu, T.; Sui, S.; Qu, S.; Qiu, C.-W. Deep-Learning-Empowered Holographic Metasurface with Simultaneously Customized Phase and Amplitude. *ACS Appl. Mater. Interfaces* **2022**, *14* (42), 48303–48310. <https://doi.org/10.1021/acsa mi.2c15362>.
- (28) Yu, X.; Zhang, H.; Zhao, Z.; Fan, X.; Hu, S.; Li, Z.; Chen, W.; Li, D.; Shi, S.; Xiong, W.; Gao, H. On the Use of Deep Learning for Computer-Generated Holography. *iScience* **2025**, *28* (5). <https://doi.org/10.1016/j.isci.2025.112507>.
- (29) Fu, Y.; Zhou, X.; Yu, Y.; Chen, J.; Wang, S.; Zhu, S.; Wang, Z. Unleashing the Potential: AI Empowered Advanced Metasurface Research. *Nanophotonics* **2024**, *13* (8), 1239–1278. <https://doi.org/10.1515/nanoph-2023-0759>.
- (30) Rogalski, A.; Kopytko, M.; Martyniuk, P. Two-Dimensional Infrared and Terahertz Detectors: Outlook and Status. *Appl. Phys. Rev.* **2019**, *6* (2), 021316. <https://doi.org/10.1063/1.5088578>.
- (31) Su, J. L.; Cai, Z. X.; Mao, Y.; Chen, L.; Yu, X. Y.; Yu, Z. C.; Ma, Q.; Huang, S. Q.; Zhang, J.; You, J. W.; Cui, T. J. Multi-Dimensional Multiplexed Metasurface for Multifunctional Near-Field Modulation by Physics-Driven Intelligent Design. *Advanced Science* **2025**, *12* (27), 2503899. <https://doi.org/10.1002/advs.202503899>.

- (32) He, Y.; Ye, S.; Han, Y.; Xun, M.; Li, Q.; Wang, R.; Gong, Q.; Li, Y. High-Speed Design of Multiplexed Meta-Optics Enabled by Physics-Driven Self-Supervised Network. *Advanced Science* **2025**, *n/a* (n/a), e09242. <https://doi.org/10.1002/advs.202509242>.
- (33) Xu, Y.; Yang, J.-Q.; Fan, K.; Wang, S.; Wu, J.; Zhang, C.; Zhan, D.-C.; Padilla, W. J.; Jin, B.; Chen, J.; Wu, P. Physics-Informed Inverse Design of Programmable Metasurfaces. *Advanced Science* **2024**, *11* (41), 2406878. <https://doi.org/10.1002/advs.202406878>.
- (34) Wei, W.; Tang, P.; Shao, J.; Zhu, J.; Zhao, X.; Wu, C. End-to-End Design of Metasurface-Based Complex-Amplitude Holograms by Physics-Driven Deep Neural Networks. *Nanophotonics* **2022**, *11* (12), 2921–2929. <https://doi.org/10.1515/nanoph-2022-0111>.
- (35) Zhou, P.; Li, Y.; Liu, S.; Su, Y. Dynamic Compensatory Gerchberg–Saxton Algorithm for Multiple-Plane Reconstruction in Holographic Displays. *Opt. Express* **2019**, *27* (6), 8958. <https://doi.org/10.1364/OE.27.008958>.
- (36) Guo, Y.; Yang, Y.; Huang, F.; Gu, J.; Ouyang, C.; Xu, Q.; Zhang, X. 3D Holographic Metasurface Design by Deep Learning with Partitioned Loss Function. *Photon. Res.* **2025**, *13* (12), 3383. <https://doi.org/10.1364/PRJ.565131>.